Results in Surfaces and Interfaces 21 (2025) 100683

Contents lists available at ScienceDirect

Results in Surfaces and Interfaces

journal homepage: www.elsevier.com/locate/rsurfi

# The effects of $TiO_2$ particles on the physico-chemical properties of polyester coatings

Ke Ren [a], Daniel Perello [b], Laura Buccoli [a], Roxana Guillen de la Cruz [a], Wahyu Wijanarko [b], Angel Gomes [c], Richard Williams [c], Nuria Espallargas [b], Anju Massey-Brooker [a], Peter J. Fryer [a], Zhenyu Jason Zhang [a,*]

[a] School of Chemical Engineering, University of Birmingham, B15 2TT, Birmingham, UK
[b] Department of Mechanical and Industrial Engineering, Norwegian University of Science and Technology, 7491, Trondheim, Norway
[c] AkzoNobel Packaging Coatings Ltd., B9 4TQ, Birmingham, UK

ARTICLE INFO

*Keywords:*
$TiO_2$ nanoparticles
Polyester coatings
Surface free energy
Wear resistance

ABSTRACT

Titanium dioxide ($TiO_2$) based surface coatings with appropriate binding matrices provide notable characteristics such as long-lasting efficacy and physico-chemical durability to minimise complex failures in a variety of applications. However, how the crystalline forms of $TiO_2$ and their distribution within matrices affect the coating characteristics remains unclear. In this research, we prepared $TiO_2$-based coatings by compositing two forms of $TiO_2$ nanoparticles (rutile and anatase) with an unsaturated polyester resin (UPR) matrix to produce $TiO_2$/UPR coatings, followed by physico-chemical characterization. Morphology and topography results revealed that the rutile nanoparticles showed a sphere-like shape, while the anatase nanoparticles had an irregular polyhedron structure. Additionally, a ring-like structure was formed on all coatings whilst coatings containing pure rutile exhibited slight agglomeration in the boundaries of rings. In contrast, anatase-containing coatings presented more agglomerates inside the rings. The consistent phenomenon was demonstrated by Raman and XRD analysis. The addition of anatase in the coatings significantly increased the surface free energy and hardness based on the wettability and nanoindentation tests. The chemical durability evaluation suggested that anatase improved the ability of chemical solution resistance of coatings by strong interaction between nanoparticles and matrix resulting from the irregular polyhedron structure and high surface free energy of the anatase nanoparticles. Excellent anti-wear performance was observed in anatase-containing coatings, implying that the nanoparticle distribution and the resulting higher hardness affected the wear-resistance of the $TiO_2$-based coatings.

## 1. Introduction

Organic/inorganic hybrid surface coatings have attracted a considerable attention due to the synergistic effect between organic and inorganic phases, which improves coating performance in diverse applications, including automotive, aerospace, electronics, and biomedical industries [1]. These hybrid systems typically comprise inorganic fillers such as silica ($SiO_2$), alumina ($Al_2O_3$), or titanium dioxide ($TiO_2$), and organic matrices such as polyacrylic acid, poly(carbonate urethane), polyurethane (PU), or polyester resins [2–7]. The combination enhances the coating's mechanical strength, thermal stability, and chemical resistance. For instance, in a study from Zhu and colleagues [4], polyacrylic acid modified graphene oxide exhibited an improvement in mechanical and chemical properties. D′ Orazio and co-workers synthesized anatase $TiO_2$ that was used alongside poly(carbonate urethane) as protective coating for the application of outdoor cultural heritage, and reported that a coating with 1 wt% of anatase $TiO_2$ nanoparticles showed good chemical durability [5]. Li et al. focused on the fabrication of graphene-reinforced waterborne Polyurethane (PU) coatings, highlighting its superior anticorrosive behavior attributed to an ideal network formation in the PU matrix that avoids permeation of foreign molecules [8]. Barroso et al. reported that particle-fillers, such as $TiO_2$, $SiO_2$, $ZrO_2$, and $Al_2O_3$, working together with polysiloxane coatings, are able to maintain a passive behavior over a broad temperature range without requiring a protective atmosphere resulting from the high-temperature stability and melting point of these fillers [6].

Despite that concern with regards its toxicity profile [9,10], titanium dioxide ($TiO_2$) is an excellent candidate due to its suitable valence band

* Corresponding author.
*E-mail address:* z.j.zhang@bham.ac.uk (Z.J. Zhang).

https://doi.org/10.1016/j.rsurfi.2025.100683
Received 8 July 2025; Received in revised form 13 October 2025; Accepted 23 November 2025
Available online 24 November 2025

and conduction band positions, long-term stability, cost-effectiveness, biocompatibility, and strong oxidizing power response [11–14]. $TiO_2$ consists of several crystalline forms, of which anatase and rutile are the two prevalent forms [15] that exhibit distinctively different properties [16]: anatase shows a greater photoactivity than rutile because of an increased level of radicals absorption on the anatase surface, causing its application in environmental purification systems, self-cleaning and antimicrobial products [17–19]. In contrast, rutile is the most thermodynamically stable form of $TiO_2$, exhibiting excellent stability and resistance to degradation, making it suitable for UV protection and weather resistance applications [20].

Within the spectrum of organic materials used in hybrid to improve the properties of $TiO_2$ coatings, unsaturated polyester resin (UPR) has recently received considerable attention. UPR synthesized based on the condensation of unsaturated diacids and saturated diols is one of the most commonly used thermosetting resins in construction, household production, and electronics [7,21]. It was reported in a previous study that addition of 4 % rutile $TiO_2$ to UPR could improve the impact strength retention rate of the coating by 29.8 % compared with the pure UPR [7]. Evora and colleagues evidenced that the introducing $TiO_2$ particles to UPR could significantly enhance the toughness of the UPR coating by as much as 57 % [22]. Moreover, Xiao and co-workers demonstrated that the tensile strength and elastic modulus of a $TiO_2$/UPR composite were increased by 47 % and 22 %, respectively, once 4 % $TiO_2$ was incorporated [23]. In addition, the impact strength of $TiO_2$/UPR coatings was increased by up to 50 % when 1.5 % anatase $TiO_2$ was used, which was attributed to the robust interfacial bonding force between the particles and the resin matrix [24].

However, although the properties of anatase and rutile $TiO_2$ have been extensively studied individually, comparative investigations of their performance within hybrid coatings remain scarce. A limited understanding of how different $TiO_2$ polymorphs interact with UPR—particularly in relation to their photocatalytic efficiency—has hampered efforts to optimize hybrid coating formulations. In this research, two crystalline forms of $TiO_2$: anatase $TiO_2$ particles and rutile $TiO_2$ particles, composited with polyester resin matrix, were chosen to construct $TiO_2$/UPR coatings on aluminum substrate plates. Depending on the different ratios of the two types of $TiO_2$ particles, the samples were named 100R (100 % rutile with UPR), 50R50A (50 % rutile and 50 % anatase with UPR), and 100A (100 % anatase with UPR). We investigated the physico-chemical properties of the coatings, including surface morphology and topography, surface roughness, surface free energy, components distribution, and coating hardness, followed by chemical durability evaluation and wear resistance test. Afterwards, the scientific implications of $TiO_2$ with polyester resin matrix on mechanical and chemical resistance are elucidated according to the nanoparticle structure and character of each crystal and the distribution of $TiO_2$ in the polymer matrix.

## 2. Materials and method

### 2.1. Preparation of hybrid $TiO_2$ surface coatings

Two types of $TiO_2$ particles, Anatase (PCN-SA, kindly donated by PCN Materials, Crete, Greece) and Rutile (Kronos 2300, Kronos Worldwide, Inc., Dallas, USA), were used as supplied. Specific ratios of $TiO_2$ particles (12 wt% anatase, 12 wt% rutile, and 6 wt% anatase mixed with 6 wt% rutile) were incorporated with an industrial coating formulation that contains primarily an unsaturated polyester resin (AkzoNobel Packaging Coatings Ltd, Birmingham, UK), respectively, followed by stirring at 4000 rpm at room temperature using a 3-bladed R1385 Propeller stirrer (IKA England Ltd., Oxford, UK) for 11 h to ensure a homogeneous distribution of the $TiO_2$ particle in the organic matrix. The resulting suspensions were subsequently coated on a Cr-free aluminum plate (Novelis, Warrington, UK) using a Wire-Bar Applicator (WC-6 Leneta Wire-Cator, Leneta, USA) and cured at 249 °C for 13 s in a hot air oven (Werner Mathis AG, Oberhasli, Switzerland).

### 2.2. Surface characterization

#### 2.2.1. Scanning electron microscopy (SEM)

A Scanning Electron Microscope (SEM) (Quanta FEI 650 FEG, Thermo Fisher Scientific, Massachusetts, USA) was utilized to study the $TiO_2$ particles alone and the $TiO_2$ particles embedded in the coating matrix. The samples of interest were coated with a thin layer of gold (approximately 5 nm) using a sputtering machine (LUXOR, Luxor Tech, Nazareth, Belgium). Back Scatter Electron (BSE) mode was chosen to distinguish the $TiO_2$ particles from the organic matrix.

#### 2.2.2. Plasma focused ion beam (PFIB)

Once an area of interest, of which the dimension of 50 μm × 10 μm × 5 μm, was established, it was sputter coated with a conducting layer of tungsten, over which cross-section feature was generated using a Plasma Focused Ion Beam (Helios 5 PFIB CXe DualBeam, Thermo Fisher Scientific, Massachusetts, USA).

#### 2.2.3. White light interferometry (WLI)

The hybrid $TiO_2$ coating samples were examined by a White Light Interferometer (Profilm3D, KLA Corporation, California, USA) using a 50× objective lens (Nikon CF Plan, Nikon Corporation, Japan), with a scanning area of 120 μm × 120 μm. The surface roughness ($S_a$) was calculated using the ProfilmOnline based on at least three measurements per sample.

#### 2.2.4. Atomic force microscopy (AFM)

An Atomic Force Microscope (FlexAFM, Nanosurf, Liestal, Switzerland) was used to establish the surface topography of the $TiO_2$ coating specimens. A contact mode cantilever (HQ:NSC36/Cr-Au, ApexProbes, UK) with a force constant of 1 N/m was utilized to image the coating surfaces under ambient conditions, with a scan size of 50 μm × 50 μm and a scanning frequency of 1 Hz. Data analysis was performed using Gwyddion software (Czech Metrology Institute, Okružní, Czech).

### 2.3. Surface free energy

Surface free energy values of the $TiO_2$ coating samples were quantified using a contact angle goniometer (Ossila Ltd, Sheffield, UK) based on the sessile drop method. Two types of liquid droplets: 10 μl of deionized water (produced by Direct-Q® 3 UV Remote Water Purification System, Merck Life Science, UK) or diiodomethane (Sigma-Aldrich, UK) was placed on the substrates of interest, of which the details were reported in a previous study [25]. Averaged data was obtained by at least 9 repeats per substrate.

In the present work study, the Fowkes equation was used to calculate surface free energy of three types of coating surface. The Fowkes' equation that relates the solid and liquid phase interactions with surface tension and contact angle is presented in Equation (1) below:

$$\sqrt{\sigma_l^D \cdot \sigma_s^D} + \sqrt{\sigma_l^P \cdot \sigma_s^P} = \sigma_l(1 + cos\,\theta) \Big/ 2 \quad (1)$$

where $\sigma_S^D$ and $\sigma_S^P$ are the dispersive and polar components of the surface energy of the solid, and $\sigma_l^D$ and $\sigma_l^P$ are the dispersive and polar components of the surface tension of the liquid.

### 2.4. Chemical characterization

#### 2.4.1. Raman microscopy

Raman spectra over different locations of the hybrid coating surface were acquired using a WiTec Confocal Raman spectrometer (Andor Technology, Oxford, UK) with a 785 nm laser excitation (Cobolt 08-NLD, HÜBNER Photonics GmbH, Germany). A 20× objective

(UPlanApo, Olympus, Japan) was used for both surface mapping and spectra recording. All Raman spectra were analyzed using the WiTec Project Data Evaluation software. For the surface mapping, a mapping size of 100 μm × 100 μm was chosen with a scanning point collection setup of 100 points per line and 100 lines per image.

#### 2.4.2. X-ray diffraction (XRD) analysis

X-ray Diffraction measurements were performed using a BRUKER D8 Advance X-ray diffractometer (Bruker, Massachusetts, USA) equipped with a Cu X-ray source (Kα wavelength of 1.5406 Å) and configured in Bragg-Brentano θ-θ geometry. A step-scan approach was used to collect the XRD pattern over a 2θ range of 20–80°, with 0.02° increments and a dwell time of 0.5 s per step.

### 2.5. Mechanical properties

Mechanical properties such as hardness and Young's modulus of the hybrid coating specimen were quantified using a Hysitron TI950 Triboindenter (Bruker, Bruker, Massachusetts, USA) equipped with a Berkovich tip. A minimum of 9 indentations were performed for each substrate.

### 2.6. Chemical durability

To evaluate their chemical durability, the hybrid coatings were exposed to aqueous solutions of different pH, following a method described in a previous study [26]. Hydrochloric acid (HCl) and sodium hydroxide (NaOH) were used to prepare solutions with pH 1 or pH 14, respectively, while de-ionized water (pH approximately 5) served as the control solution. Water contact angles of hybrid $TiO_2$ coating samples were measured before and after exposure to these solutions. The coatings underwent specific exposure treatment durations of 0.5 h, 4 h, 8 h, 16 h, and 48 h.

### 2.7. Adhesion to the supporting substrate

To evaluate the adhesion of the $TiO_2$-based coatings to the supporting substrate, a scratch was performed on the coating surface under controlled loading conditions at a scratch distance of 5 mm (constant loads of 1000 mN, 2000 mN, and 5000 mN; incremental loads of 1000–2000 mN and 1000–3000 mN). The scratches were analyzed by an Optical Microscope (BX53M, Olympus, Japan) and Infinite Focus Microscopy (Alicona G4, Bruker, Chicago, USA), based on which the mechanical failures including failure modes (following guideline presented in Table 1), scratch depths, scratch area, and scratch volume were concluded.

### 2.8. Statistical analysis

All data included in this work was calculated from more than three independent experiments and are presented as mean value ± standard deviation (mean ± SD). Significant differences among groups were determined using a one-way analysis of variance (ANOVA) and *t*-test analysis. Significance was defined as *p < 0.05, **p < 0.01, ***p < 0.001 and ****p < 0.0001.

**Table 1**
Failure Types and their characteristics in hybrid coatings.

| Failure type | Characteristics |
|---|---|
| **Critical Load 1 (Lc1):** Cohesive failure, | Visible damage, microcracks |
| **Critical Load 2 (Lc2):** Adhesive failure, | Partial delamination, some substrate exposed |
| **Critical Load 3 (Lc3):** Catastrophic failure | Total delamination, substrate exposed |

## 3. Results and discussion

### 3.1. The effects of $TiO_2$ particles on polyester coating morphology and topography

Fig. 1 presents the morphology of the $TiO_2$ particles used, the hybrid $TiO_2$ coatings, and the cross-section of the corresponding coatings specimen. The rutile nanoparticles exhibited a spherical morphology with an approximate particle size of 509 ± 51 nm. In contrast, the anatase nanoparticles showed irregularly shaped clusters, despite the fact that individual anatase particles were smaller than the rutile ones (the particle size: 40 ± 9 nm) (Fig. 1a). Regarding the surface morphology of the coatings (Fig. 1b), all the $TiO_2$ particles with lacquers formed a grain-like structure separated by well-defined grain boundaries based on the optical micrograph and SEM images. 100R showed a more uniform $TiO_2$ distribution with a slight agglomeration in the grain boundary regions (BSE images). In contrast, 50R50A and 100A presented more nanoparticle agglomerates outside the grain boundary regions but inside the grain-like structure. EDS measurement in Fig. S1: Ti was not detected in the grain boundary regions. Furthermore, the differences in $TiO_2$ nanoparticle morphology are evidenced by the images acquired from the cross-section regions (BFIB images): small rutile particles in sample 100R (diameter: ca. 500 nm, refer to the yellow marks), large anatase clusters which are likely attributed to the high anatase agglomeration in sample 100A and a combination of rutile and anatase particles in sample 50R50A.

Fig. 2 shows the surface topography and area roughness of three different $TiO_2$ coatings, showing a consistent cluster and boundary structure also seen in the results from Fig. 1. Based on the AFM results, pure anatase $TiO_2$ particles adhered to the polyester resin matrix, also demonstrated by the roughness test made by the white light interferometer (WLI) in Fig. 2d. The roughness of 100A was 2.62 ± 0.67 μm, significantly larger than that of 100R (1.31 ± 0.44 μm) and 50R50A (1.48 ± 0.45 μm).

### 3.2. Chemical characterization

The chemical composition and homogeneity, as well quality of surface coverage, were measured by Raman microscope and X-ray diffraction (XRD), of which the results are presented in Fig. 3. The Raman spectrum of anatase particles (Fig. 3a) shows characteristic peaks that correspond to $E_g(1)$, $E_g(2)$, $B_{1g}$, $A_{1g}$, and $E_g(3)$ at 138 $cm^{-1}$, 197 $cm^{-1}$, 398 $cm^{-1}$ 518 $cm^{-1}$ and 641 $cm^{-1}$, respectively, which is consistent with a previous study [27]. Moreover, the rutile Raman peaks of $B_{1g}$ (148 $cm^{-1}$), $E_g$ (449 $cm^{-1}$) as well as $A_{1g}$ (614 $cm^{-1}$) in rutile particles represented the rutile distribution in coatings [28]. The Raman spectrum of sample 100A (Fig. 3b) exhibits characteristic anatase peaks at $B_1g$ (421 $cm^{-1}$), $A_1g$ (520 $cm^{-1}$), and Eg (642 $cm^{-1}$), consistent with the fingerprint of anatase $TiO_2$. However, compared with pure anatase powders, the intensity of the prominent Eg(1) band (~144 $cm^{-1}$) in the coatings was markedly reduced, in agreement with previous reports [29, 30]. This attenuation can be ascribed to several factors. For instance, coatings are known to suppress Raman intensities through substrate interactions, optical absorption, scattering, and the reduced effective sampling volume [29]. Moreover, when $TiO_2$ nanoparticles are dispersed within a polymer matrix, the optical path of both the incident and scattered light may be blocked or attenuated, further diminishing the Raman signal [30]. In contrast, the Raman spectrum of sample 100R displayed peaks at $B_1g$ (143 $cm^{-1}$), Eg (447 $cm^{-1}$), and $A_1g$ (610 $cm^{-1}$), confirming the presence of rutile within the coatings, albeit with relatively lower intensity compared to pure rutile powders. Whereas the Raman magnitude of such peaks was seen to be small (the Ramen magnitude of $B_{1g}$, $E_g$ and $A_{1g}$: 4190, 3930 and 3920, respectively) compared to the peaks in sample 50R50A (the Ramen magnitude of $B_{1g}$, $E_g$ and $A_{1g}$: 5980, 4000, and 4020, respectively). Furthermore, it was observed that the magnitude of signal peaks, e.g. $B_{1g}$, acquired from

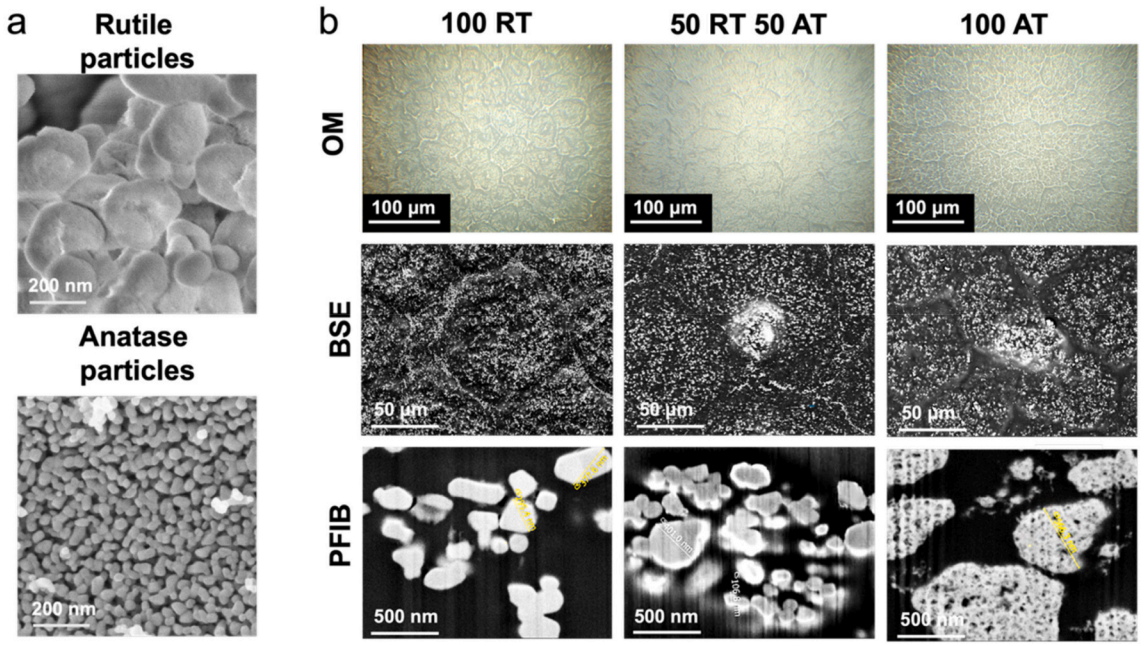


**Fig. 1.** Morphology of (a) $TiO_2$ particles: rutile (up) and anatase (bottom), and (b) TiO2 incorporated coatings: Coating constructures measured by optical microscopy (OM, top line), scanning electron microscope (SEM) Back Scatter Electron (BSE) mode (middle line) and cross-section microstructure of $TiO_2$ coatings through plasma focused ion beam (PFIB) (bottom line). The white dots in BSE and BFIB images refer to the $TiO_2$ particles, and the yellow marks show the size of $TiO_2$ nanoparticles, respectively.

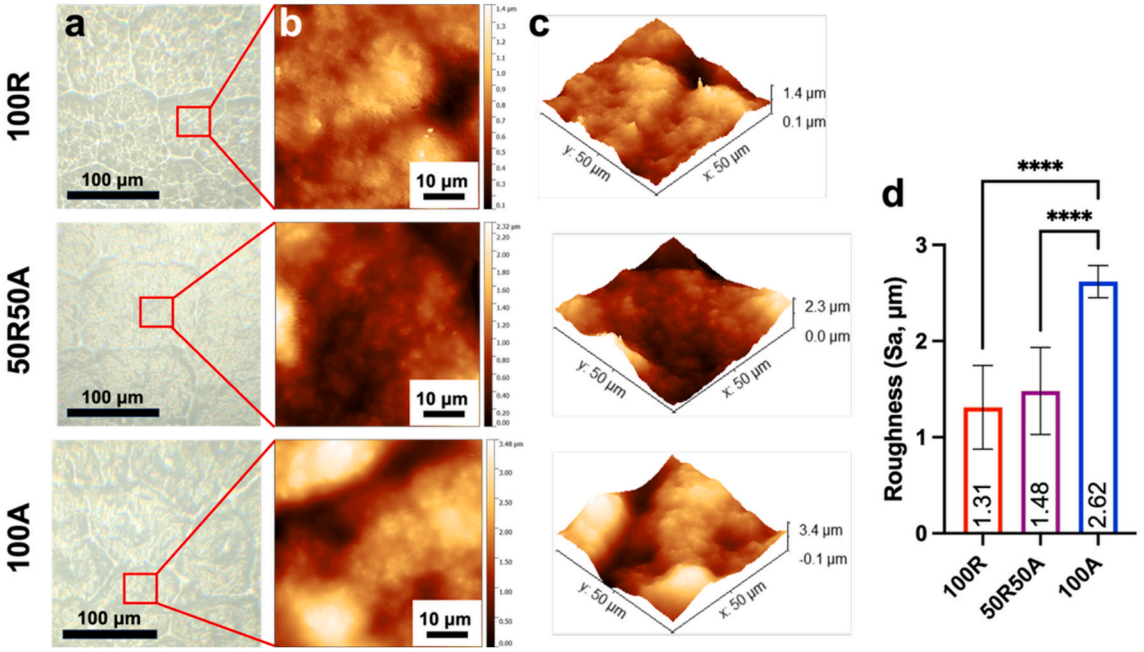


**Fig. 2.** Surface morphology of variable $TiO_2$ coating measured by (a) Raman microscope and (b) AFM. (c) 3D topographical profiles tested by AFM and (d) the surface area roughness measured by WLI. The error bars represent the standard deviation (n = 9, mean ± SD). ****p < 0.0001: compared with the group of 100R (one-way ANOVA).

100A sample is greater than that in 50R50A samples. This could be due to the influence of the size or agglomeration of $TiO_2$ particles inside coatings, which has been studied and demonstrated in a large number of works [28,31,32]: in theory, the Raman scattered radiation travels inside the sample through a diffuse reflectance scattering mechanism. In some cases, larger particles or higher agglomeration scatter more photons and provide greater scattering volume, enhancing the overall Ramen signal magnitude. The Raman results above suggest more anatase $TiO_2$ particle agglomeration in 100A, less rutile particle aggregation in 100R compared to 50R50A. This supports the observation from the PFIB results in Fig. 1 and Fig. S2.

The X-ray diffraction data of the $TiO_2$ particles and three coating specimens are shown in Fig. 2c and d. The diffraction peaks of anatase particles such as (101) at 25.33°, (004) at 37.81°, (200) at 48.05°, and (211) at 55.06° (Fig. 2c) are consistent with the reference pattern of anatase $TiO_2$ (ICDD card No. 00-021-1272), confirming that the powders

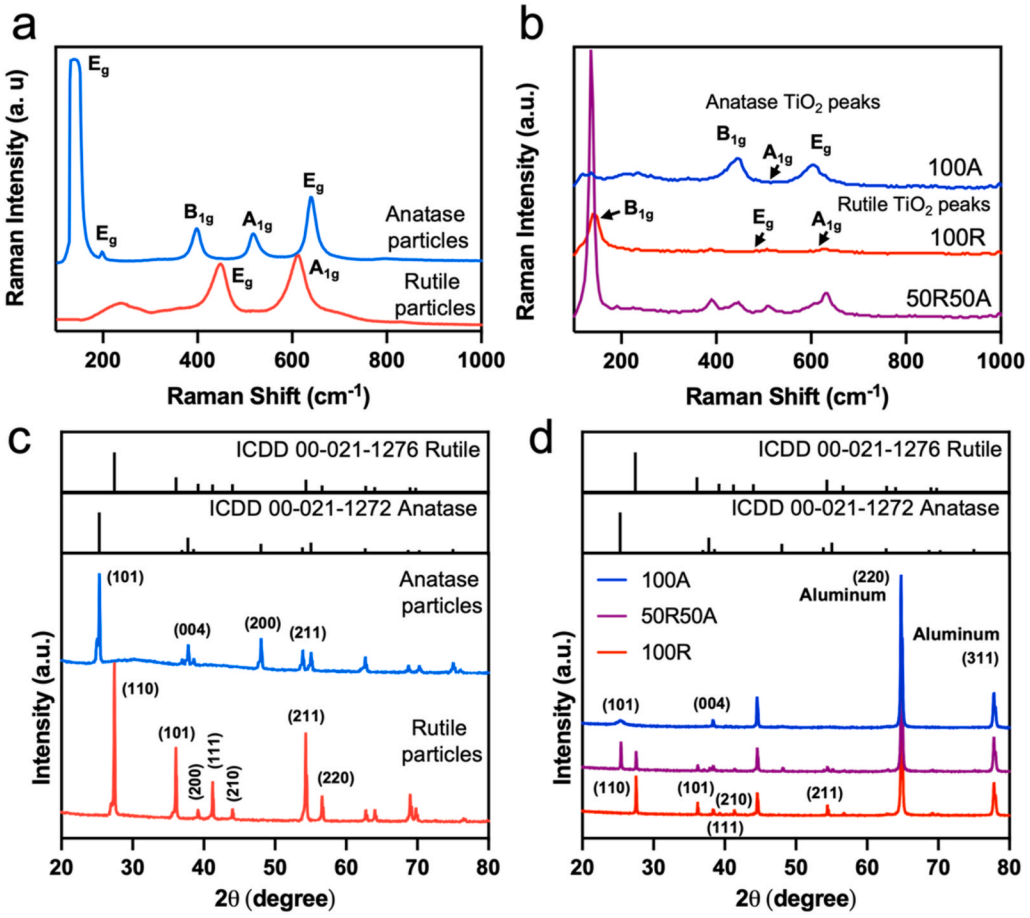


**Fig. 3.** The Raman spectra of (a) $TiO_2$ particles and (b) three coatings based on $TiO_2$ particles and XRD results of (c) $TiO_2$ particles and (d) three coatings.

used in this study were phase-pure anatase. In contrast, the characteristic reflections of rutile particles, including (110) at 27.44°, (101) at 36.07°, (200) at 39.17°, (111) at 41.23°, (210) at 44.03°, (211) at 54.32°, and (220) at 56.63°, were identified by comparison with the rutile reference pattern (ICDD card No. 00-021-1276). In Fig. 3d, three peaks, namely (101), and (004) were observed on the 100A coating, which confirms that the $TiO_2$ particles incorporated exhibit a pure anatase phase structure. However, a similar trend was observed in the XRD patterns, where the anatase-incorporated coating (100A) exhibited a reduced intensity of the characteristic (101) reflection compared to pure anatase powders. This reduction is likely attributed to the thin-film geometry [33] and substrate influence [34], which attenuate the relative diffraction intensity in coatings compared with powders. On the contrary, five different peaks, including (110) at 27.55°, (101) at 36.19°, (111) at 41.35°, and (211) at 54.42°, were identified in the XRD spectrum of 100R coating, evidencing the rutile form of the $TiO_2$ particles [35,36]. It is not unexpected to observe a range of peaks, contributed by both rutile and anatase, in the 50R50A coating sample. The XRD results confirm not only the nature of the $TiO_2$ particles used, but that the coating preparation process does not affect the crystalline form of $TiO_2$.

### 3.3. *Surface free energy of the $TiO_2$ based coatings*

The Equilibrium Contact Angle (ECA) values of water, reflecting the surface water wettability, on $TiO_2$ coatings are summarised in Fig. 4a. All coatings showed water wettability within a close range, with a

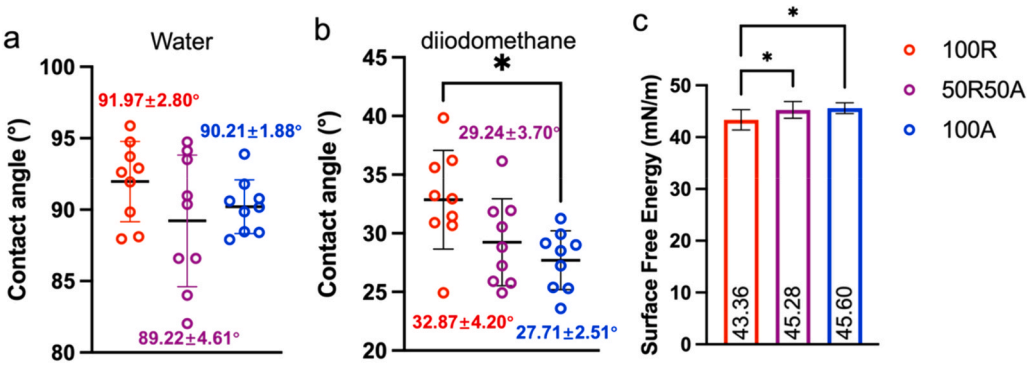


**Fig. 4.** The contact angle of different $TiO_2$ coatings (a) against water and (b) against diiodomethane. (c) The surface free energy of different $TiO_2$ samples. The error bars represent the standard deviation (n = 9, mean ± SD). *p < 0.05: compare with the group of 100R (One-way ANOVA).

contact angle of approximately 90° (91.9 ± 2.8°, 89.2 ± 4.6°, and 90.2 ± 1.9° for 100R, 50R50A, and 100A, respectively). To quantify the surface free energy (SFE) of the coatings and elucidate the interface characteristics for each composition, ECA of diiodomethane was measured (Fig. 4b), of which the results were used to calculate the surface free energy of the coatings (Fig. 4c). Diiodomethane was used to probe the non-polar interactions on the $TiO_2$ coatings surface, including Van der Waals forces and solvent-mediated phenomena such as hydrophobic attraction [25], while the polar interactions (electrostatic interaction or hydrogen bonds) were evaluated through the ECA of water [37]. Although the same polymeric matrix was used for all three coatings, the 100R coatings showed a diiodomethane ECA value of 27.7 ± 2.5° that is higher than that of the 50R50A coatings (29.2 ± 3.7°) and the 100A coatings (32.8 ± 4.2°). It is very probable that the SFE of the $TiO_2$ based coatings is primarily influenced by the characteristics of the $TiO_2$ phases. SFE was found to increase marginally with the increase of anatase ratio in the coating (43.36 ± 1.97, 45.28 ± 1.61 mN/m, and 45.60 ± 1.04 for 100R, 50R50A, and 100A, respectively).

Fig. 5 shows the wettability and surface free energy as a function of the $TiO_2$ coatings, and the relation between surface free energy and surface roughness. The diiodomethane contact angle on $TiO_2$ coatings decreases (Fig. 5a) as the fraction of anatase increases, which results in an increased dispersive component of surface free energy (Fig. 5b) by 5.11 %. This implies that the anatase nanoparticles might be able to enhance the dispersive component of the surface energy, which is consistent with a previous study [38]. Fig. 5c and d show surface free energy (either total, disperse, or polar component) as a function of the surface roughness, which advises that SFE is independent of surface roughness. Therefore, the different $TiO_2$ phases, rather than coating surface roughness, likely play the greatest role in the surface free energy of hybrid coatings although the factor is not much noticeable [39].

### 3.4. Mechanical properties of the coatings

The effect of including $TiO_2$ nanoparticles in polyester resin on the hardness and reduced Young's modulus of the surface coating is presented in Fig. 6. Nanoindentation results show that the value of hardness

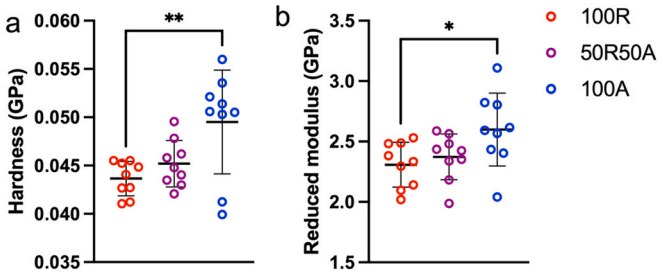


**Fig. 6.** The (a) hardness and (b) reduced modulus of different $TiO_2$ coatings. The error bars represent the standard deviation (n = 9, mean ± SD, *p < 0.05 and **p < 0.01: compared with the group of 100R, One-way ANOVA).

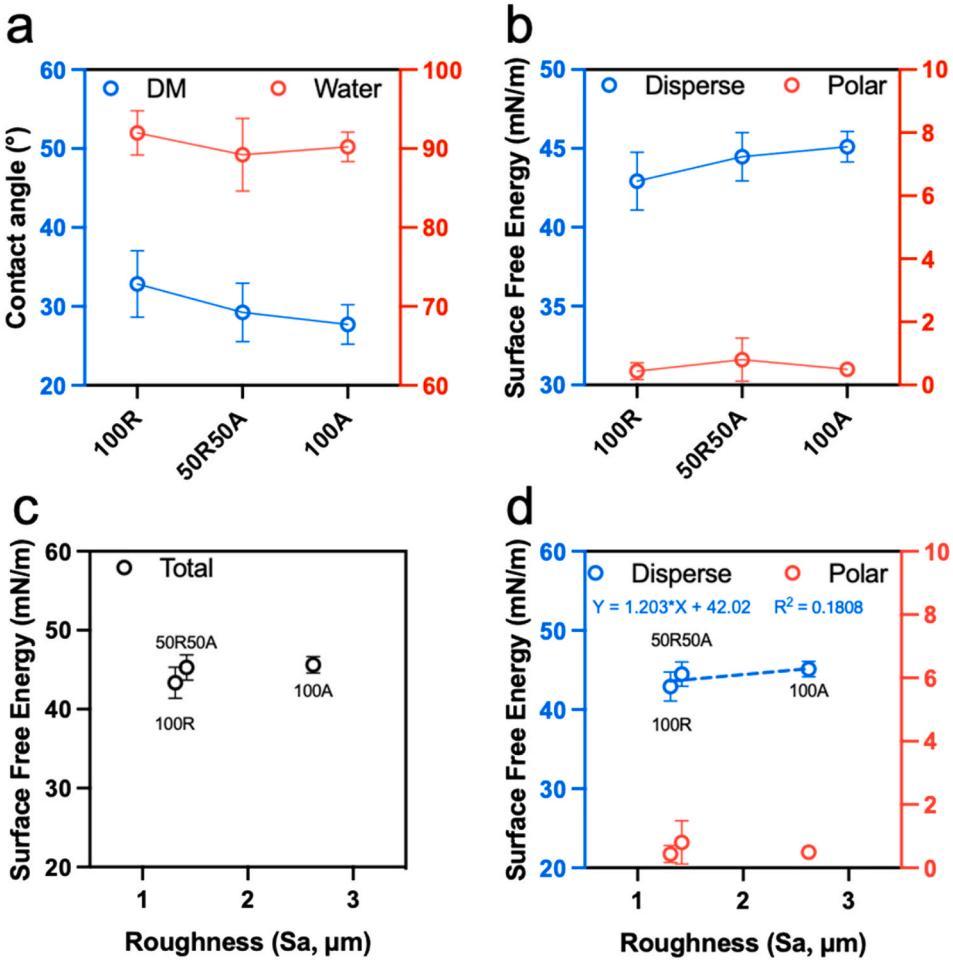


**Fig. 5.** (a) Contact angle values of water and diiodomethane acquired on $TiO_2$ coatings. (b) Disperse and polar components of surface free energy of the three $TiO_2$ samples. (c) The relation between surface roughness and surface free energy. (d) The relation between roughness and disperse and polar components. The error bars represent the standard deviation (n = 9, mean ± SD).

of 100A, 0.050 ± 0.005 GPa, was significantly greater than that of 100R (0.044 ± 0.002 GPa) and 50R50A (0.045 ± 0.002 GPa), respectively. The total replacement of rutile by 100 % anatase resulted in a 12 % increase in the hardness of the coating. The same enhancing effect was observed with the reduced Young's modulus result, whereby the 100A coating presents a reduced Young's modulus of 2.599 ± 0.302 GPa, which is greater than that for 100R (2.308 ± 0.185 GPa). We conclude that the presence of anatase particles could enhance the mechanical performance of the $TiO_2$ coatings. The benefit is likely attributed to the anatase particles could act as an obstacle to plastic deformation of the polyester resin matrix: the anatase nanoparticles have excessive dangling bonds which allows for strong interactions with the polyester matrix, leading to a strong interface between the nanoparticles and the matrix [40], which was also supported by previous research [41], that reported that nickel nanocomposite coatings containing anatase nanoparticles showed a higher hardness rate compared with those containing rutile microparticles. The role of $TiO_2$ particle distribution and agglomeration within the polyester resin matrix (Fig. 1b and S2) may also contribute to the observed mechanical response. In the 100A coating, anatase nanoparticles formed numerous clusters (Fig. S2c), which can act as rigid filler domains and enhance the local resistance to indentation. Such clustered regions are capable of locally increasing stiffness and hardness, despite the non-uniform dispersion of the particles. A similar phenomenon was reported by Rovera et al., who demonstrated that coating regions with more pronounced aggregation or clustering of rigid nanoparticles acted as locally reinforced domains, resulting in higher measured nanomechanical properties such as hardness and stiffness [42].

### 3.5. Chemical durability

Coatings based on $TiO_2$ particles are deployed in a wide range of sectors such as biomedical industry, food packaging, agriculture [43–47], which requires an exceptional stability and durability when being exposed to challenging environmental conditions. A chemical durability evaluation for the coatings that are consisted of $TiO_2$ particles and polyester resin was carried out against aqueous solutions of different pH values, whereby the water contact angle (WCA) of the coatings was measured as a function of pH condition and exposure time, of which the results are presented in Fig. 7.

It is apparent that the WCA of the 100R coating changed upon exposure to the testing liquids. For instance, the water contact angle of 100R reduced upon exposure to acidic environment (pH = 1) from 87.3 ± 0.9° to 83.6 ± 0.6° after 0.5 h, but from 88.7 ± 3.1° to 76.0 ± 0.7°after 8 h, which highlights the significance of resistance against chemicals. After immersion in deionized water, 100R coating deterioration was observed under the treatment for 8 h and 48 h, after which the ECAs raised from 84.9 ± 3.0° to 95.6 ± 0.9° and from 85.0 ± 0.9° to 91.4 ± 1.5°, respectively. Compared with previous liquids, the alkaline solution (pH = 14) damaged the pure rutile coating more significantly: all the contact angle values were reduced after specific treatment periods, especially after 48 h, the ECA went down almost 30 % from 83.8 ± 1.3° to 60.9 ± 6.9°. The chemical durability of 50R50A presented is between that of 100A and 100R coatings with no significant difference in ECA observed before and after exposure to HCl and water. However, NaOH exposure resulted in a significant reduction in ECA on the coating surface across nearly all treatment durations. As for the 100A sample, the value of ECA significantly dropped down from 89.8 ± 3.2° to 80.7 ± 0.8°after 16 h). Beyond this, no noticeable changes were observed.

It is worth noting that 100A coating exhibited the best performer in terms of chemical durability because of its consistent water contact angle upon exposure to the testing liquids, despite that there was a slight ECA reduction after 16 h exposure to the alkaline environment (reduced from 89.8 ± 3.2°to 80.7 ± 0.8°). The excellent chemical durability of 100A coating is likely attributed to the distinct nature between rutile and anatase nanoparticles in the polyester resin matrix. The anatase nanoparticles have slightly greater surface free energy than rutile particles, which was observed in section 3.3 (Figs. 4 and 5), and was also

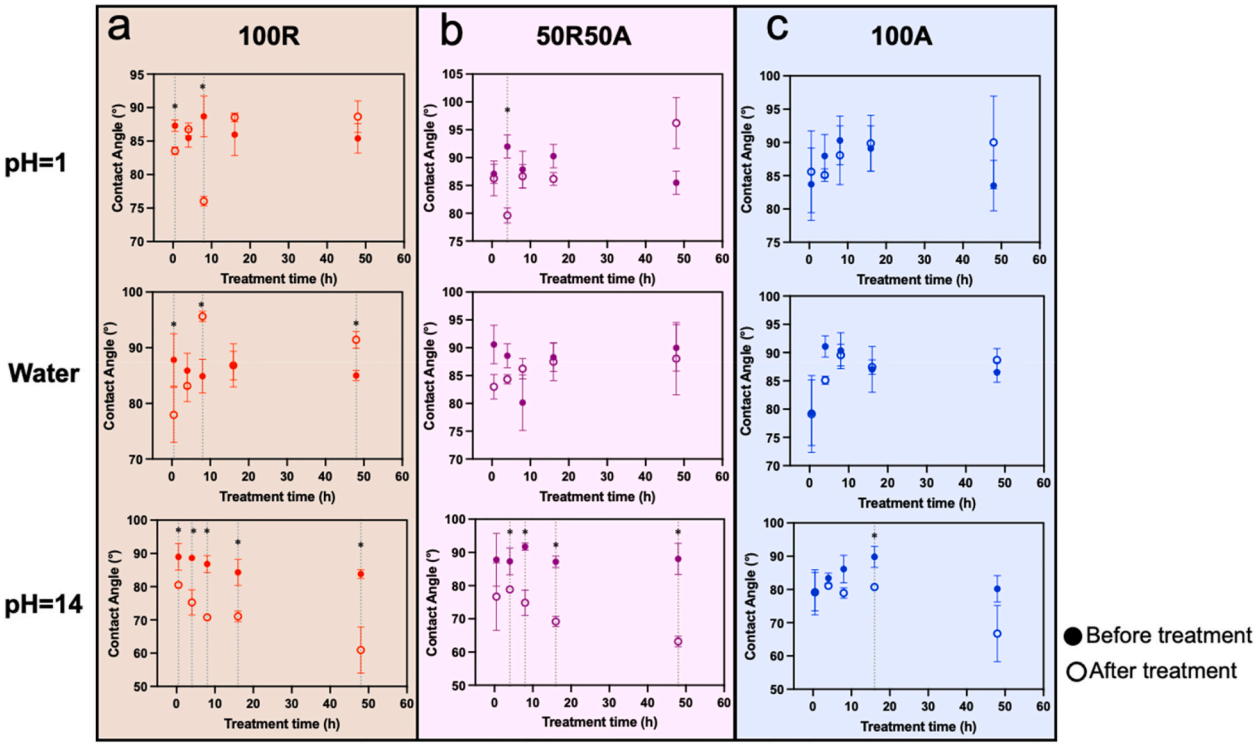


**Fig. 7.** The chemical durability of different $TiO_2$ coatings under acidic (pH = 1) water and alkaline (pH = 14) environments: (a) 100R, (b) 50R50A and (c) 100A. The error bars represent the standard deviation (n = 3, mean ± SD). *p < 0.05: comparison between the contact angle values before and after treatment at the same time point (*t*-test).

reported by other studies [16]. This is likely one of the reasons anatase particles possess a strong interaction between the anatase nanoparticles and the polyester matrix [41]. Additionally, Shoaib et al. demonstrated that the anatase nanoparticles have a defect-rich surface with excessive dangling bonds which allows for strong interactions with the polyester matrix, resulting in a robust interface between the nanoparticles and the matrix [40]. Consequently, this strong interaction resulted in the resistance of corrosive liquid permeating into the coatings [48].

### 3.6. Adhesion performance of $TiO_2$ coatings

The mechanical durability of the $TiO_2$ coatings was evaluated by a set of scratch tests under two different testing conditions: constant loading at 1000, 2000, and 5000 mN, and incremental loading at 1000–2000 and 1000–3000 mN. The results are shown in Fig. 8, whereby Fig. 8a & b present the scratch test under constant load and Fig. 8c, d, and 8e show the incremental load test results. The maximum scratch depth on all coatings increased once the constant normal load was enhanced from 1000 mN to 5000 mN, e.g. approximately 5 μm under 1000 mN; 11 μm under 2000 mN, and 16 μm under 5000 mN. Lc1 failure type was observed for all samples under 1000 mN normal load, whereas a combination of Lc2 + Lc3 failure type was found on 100R coating surface under 2000 mN, implying a worse coating adhesion of pure rutile nanoparticle coatings compared with that of anatase particle-containing coatings (50R50A and 100A), on which only Lc2 failure occurred. Mechanical properties of all three coatings deteriorated under a normal constant load of 5000 mN, showing a Lc3 failure type, which is likely because the applied load (5000 mN) exceeded the limits of the mechanical endurance of the coatings (Additional details regarding the 3D scratch profiles can be found in Fig. S3). With regards the coating adhesion under an incremental load from 1000 mN to 2000 mN (Fig. 8c), a increased max scratch depth was observed on 100A specimen (9.93 ± 0.45 μm), in comparison to that on the 100R coating (8.26 ± 0.61 μm). This evidences that the maximum load of 2000 mN still could not break all coatings and only slight tracks remained. It manifests that the normal load of 2000 mN is likely the threshold to produce cracks and debris, which could result in a mechanical failure.

To quantitatively analyze the magnitude of adhesion of the coating to the supporting substrate (Fig. 8d and e), the values of the scratch area and volume were calculated under the incremental load of 1000 mN–3000 mN. Based on the scratch area and volume results, we concluded that the coating containing anatase (100A) shows a greater wear resistance than the coatings containing rutile (100R): scratch area and scratch volume are 0.24 ± 0.03 $\mu m^2$ and 1.27 × $10^5$ $\mu m^3$ for the 100A sample, and become 0.21 ± 0.02 $\mu m^2$ and 1.34 × $10^5$ $\mu m^3$ for the 50R50A specimen, both of which are considerably less than those (0.29 ± 0.03 $\mu m^2$ and 1.84 × $10^5$ $\mu m^3$, respectively) acquired on the 100R coating.

The wear performance of the coatings could be affected by their mechanical properties, such as hardness and particle distribution, and by their chemical composition, e.g. inclusion of anatase or rutile particles [49]. It is anticipated that the coatings containing anatase (100A and 50R50A), with a great hardness (Fig. 6), could inhibit the plastic deformation under a high loading force, therefore exhibit an enhanced wear resistance [41]. Moreover, the agglomeration of rutile nanoparticles located in the peripheral regions of nanoparticle clusters in 100R (Fig. 1b, BSE image, red circle) likely deteriorated the wear performance further. A similar experimental phenomenon has been found in the research by Aliofkhazraei et al. [49], who reported that higher agglomeration of nanoparticles in the valleys of the coating resulted in the uneven force subjecting conditions on coatings, further leading to worse wear resistance.

### 3.7. Limitations

In this study, the physico-chemical characterization of $TiO_2$/UPR coatings prepared with anatase and rutile particles was investigated. Nonetheless, certain limitations remain to be addressed in future work. For example, additional chemical characterization techniques such as FTIR and XPS should be employed to gain deeper insights into the chemical composition and structural features of the $TiO_2$/UPR coatings. Meanwhile, chemical durability was evaluated primarily under acidic and alkaline environments. However, it is well established that $TiO_2$ can exhibit strong photocatalytic activity under UV irradiation, which may induce gradual degradation of the polymeric matrix. Such photoinduced degradation could compromise the long-term stability of the coatings in

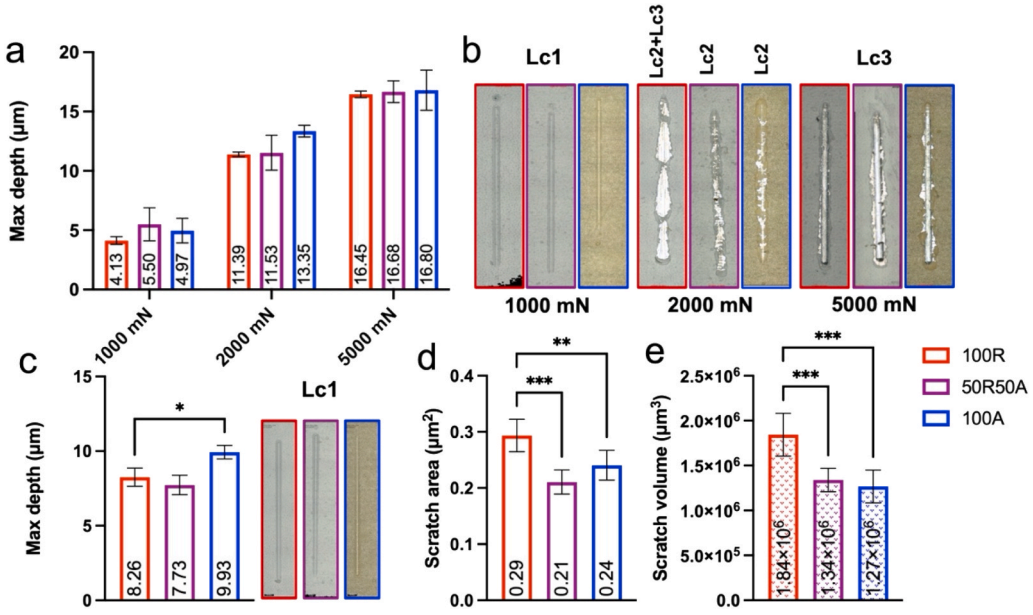


**Fig. 8.** The adhesion evaluation for different $TiO_2$ coatings. (a) The maximum penetrated depth of $TiO_2$ coatings by Berkovich tip with constant normal loads: 1000 mN, 2000 mN and 5000 mN. (b) the relative scratches from constant normal load testing. (c) The maximum penetrated depth with incremental normal loads from 1000 mN to 2000 mN and the relative scratches. (d) The scratch area and (e) the scratch volume with incremental normal load from 1000 mN to 3000 mN of different $TiO_2$ coatings. The error bars represent the standard deviation (n = 3, mean ± SD). *p < 0.05: compared with the group of 100R (One-way ANOVA).

outdoor applications and may also lead to the release of $TiO_2$ nanoparticles into the environment, raising potential ecological and health concerns. Future investigations will therefore focus on accelerated weathering and UV exposure tests to more comprehensively evaluate the photo-durability of the coatings and to assess nanoparticle release under realistic service conditions. Moreover, the effect of varying anatase/rutile ratios on the physico-chemical durability warrants systematic investigation, as this work focused only on a 1:1 ratio. The absence of a control coating prepared from UPR without $TiO_2$ incorporation is also another limitation. While the rutile-based coating (100R) was considered as a practical reference due to its availability as a mature commercial product from our industrial collaborator, it does not fully isolate the effect of $TiO_2$ incorporation on physico-chemical properties. Including a $TiO_2$-free UPR coating would have enabled more precise quantification of the contribution of $TiO_2$. Future work will therefore incorporate such a control sample to provide a more rigorous comparison.

## 4. Conclusions

In this study, we investigate how the distribution and crystalline composition of anatase and rutile $TiO_2$ nanoparticles influence the physico-chemical properties of hybrid coatings based on polyester resin. Particular attention is given to understanding how variations in particle dispersion and anatase/rutile affect coating performance and durability when incorporated into an unsaturated polyester resin matrix. The morphological characteristics of the coating revealed a sphere-like shape for the rutile nanoparticles, but irregular polyhedron clusters for anatase nanoparticles agglomeration. A repetitive ring-like structure was observed on the surfaces of all coatings, for the rutile-based coatings, $TiO_2$ particles exhibited slight agglomeration primarily in the boundary areas of these ring-like structures. In contrast, anatase-containing coatings displayed more pronounced nanoparticle agglomeration within ring-like regions. In addition, the anatase coatings exhibited greater nanoparticle aggregation within the polyester matrix compared to rutile hybrid coatings, as confirmed by Raman and XRD analyses. These analyses also verified both the crystalline nature of the $TiO_2$ nanoparticles used and confirmed that the coating preparation process did not affect their crystalline structure. Surface wettability and nanoindentation tests demonstrated that the addition of anatase in the coatings slightly increased the surface free energy by 5.17 % and hardness by 13.64 %. The chemical durability analysis showed that anatase improved the chemical resistance of the coatings. The scratch results revealed a superior anti-wear performance of anatase-containing coatings, implying that the coating hardness and nanoparticle distribution likely played a crucial role, i.e. the agglomeration of the rutile nanoparticles located within the ring-like shape boundary regions in the coating may cause uneven force conditions, along with low hardness, deteriorating the wear performance.

The demonstrated improvements in surface free energy, chemical stability, mechanical properties, and wear resistance suggest that anatase/UPR hybrid coatings hold strong potential for real-world applications as protective or functional coatings. Such properties are especially relevant for use in high-touch surfaces, packaging, or building materials, where enhanced durability and surface performance are critical.

Based on the results above, future improvements of $TiO_2$/UPR hybrid coatings could be achieved by enhancing nanoparticle dispersion or incorporating additional functional fillers such as Ag or ZnO nanoparticles to tailor the performance. Such coatings hold promise for use in protective and functional applications, including construction, marine, and automotive sectors, where durability, photocatalytic self-cleaning, and antimicrobial properties are highly desirable.

## CRediT authorship contribution statement

**Ke Ren:** Writing – review & editing, Writing – original draft, Validation, Software, Methodology, Investigation, Formal analysis, Data curation. **Daniel Perello:** Writing – review & editing, Writing – original draft, Validation, Software, Methodology, Formal analysis, Data curation. **Laura Buccoli:** Validation, Methodology, Formal analysis, Data curation. **Roxana Guillen de la Cruz:** Writing – original draft, Validation, Methodology, Formal analysis, Data curation. **Wahyu Wijanarko:** Validation, Methodology, Formal analysis, Data curation. **Angel Gomes:** Methodology. **Richard Williams:** Validation. **Nuria Espallargas:** Writing – review & editing, Writing – original draft, Visualization, Validation, Supervision, Project administration, Methodology, Investigation, Conceptualization. **Anju Massey-Brooker:** Writing – review & editing, Writing – original draft, Visualization, Validation, Supervision, Project administration, Methodology, Conceptualization. **Peter J. Fryer:** Writing – review & editing, Writing – original draft, Visualization, Validation, Supervision, Project administration, Methodology, Conceptualization. **Zhenyu Jason Zhang:** Writing – review & editing, Writing – original draft, Visualization, Validation, Supervision, Project administration, Methodology, Investigation, Conceptualization.

## Declaration of competing interest

The authors declare that they have no known competing financial interests or personal relationships that could have appeared to influence the work reported in this paper.

## Acknowledgments

We acknowledge financial support from the UK Research & Innovation (Horizon Europe Guarantee scheme, 10066793), the European Union's Horizon Europe research and innovation programme under Grant Agreement No 101058422 (SUPREME project), and Engineering and Physical Science Research Council (EP/V029762/1). The authors thank PCN Materials and AkzoNobel for providing anatase particles and $TiO_2$ coating samples, respectively. The PFIB images were performed by Hamid Khanmohammadi at the NTNU-PFIB lab that is a part of the SMART-H Infrastructure financially supported by the Research Council of Norway (project 296197) and NTNU.

## Appendix A. Supplementary data

Supplementary data to this article can be found online at https://doi.org/10.1016/j.rsurfi.2025.100683.

## Data availability

Data will be made available on request.

## References

[1] Liu, F., Liu, A., Tao, W., Yang, Y., 2020. Preparation of UV curable organic/inorganic hybrid coatings-a review. Prog. Org. Coating. 145, 105685. https://doi.org/10.1016/j.porgcoat.2020.105685.
[2] Frigione, M., Lettieri, M., 2018. Novel attribute of organic-inorganic hybrid coatings for protection and preservation of materials (stone and wood) belonging to cultural heritage. Coatings 8. https://doi.org/10.3390/coatings8090319.
[3] Peng, T., Xiao, R., Rong, Z., Liu, H., Hu, Q., Wang, S., Li, X., Zhang, J., 2020. Polymer nanocomposite-based coatings for corrosion protection. Chem. Asian J. 15, 3915–3941. https://doi.org/10.1002/asia.202000943.
[4] Zhu, M., Li, S., Sun, Q., Shi, B., 2022. Enhanced mechanical property, chemical resistance and abrasion durability of waterborne polyurethane based coating by incorporating highly dispersed polyacrylic acid modified graphene oxide. Prog. Org. Coating. 170, 106949. https://doi.org/10.1016/j.porgcoat.2022.106949.
[5] D'Orazio, L., Grippo, A., 2015. A water dispersed titanium dioxide/poly(carbonate urethane) nanocomposite for protecting cultural heritage: preparation and properties. Prog. Org. Coating. 79, 1–7. https://doi.org/10.1016/j.porgcoat.2014.09.017.

[6] Barroso, G., Li, Q., Bordia, R.K., Motz, G., 2019. Polymeric and ceramic silicon-based coatings-a review. J. Mater. Chem. A. 7, 1936–1963. https://doi.org/10.1039/c8ta09054h.

[7] Jiang, C., Jin, C., Wei, M., Yan, S., Chen, D., 2018. Mechanical and thermal properties improvement of unsaturated polyester resin by incorporation of TiO2 nanoparticle surface modified with titanate. Mater. Res. Express 5. https://doi.org/10.1088/2053-1591/aadc42.

[8] Faccini, M., Bautista, L., Soldi, L., Escobar, A.M., Altavilla, M., Calvet, M., Domènech, A., Domínguez, E., 2021. Environmentally friendly anticorrosive polymeric coatings. Appl. Sci. 11. https://doi.org/10.3390/app11083446.

[9] Manzoor, Q., Sajid, A., Ali, Z., Nazir, A., Sajid, A., Imtiaz, F., Iqbal, S., Younas, U., Arif, H., Iqbal, M., 2024. Toxicity spectrum and detrimental effects of titanium dioxide nanoparticles as an emerging pollutant: a review. Desalin. Water Treat. 317, 100025. https://doi.org/10.1016/j.dwt.2024.100025.

[10] Chandoliya, R., Sharma, S., Sharma, V., Joshi, R., Sivanesan, I., 2024. Titanium dioxide nanoparticle: a comprehensive review on synthesis, applications and toxicity. Plants 13. https://doi.org/10.3390/plants13212964.

[11] Zhang, J., Zhou, P., Liu, J., Yu, J., 2014. New understanding of the difference of photocatalytic activity among anatase, rutile and brookite TiO2. Phys. Chem. Chem. Phys. 16, 20382–20386. https://doi.org/10.1039/c4cp02201g.

[12] Kumaravel, V., Nair, K.M., Mathew, S., Bartlett, J., Kennedy, J.E., Manning, H.G., Whelan, B.J., Leyland, N.S., Pillai, S.C., 2021. Antimicrobial TiO 2 nanocomposite coatings for surfaces , dental and orthopaedic implants. Chem. Eng. J. 416, 129071. https://doi.org/10.1016/j.cej.2021.129071.

[13] Fu, G., Vary, P.S., Lin, C., 2005. Anatase TiO 2 Nanocomposites for Antimicrobial Coatings, pp. 8889–8898.

[14] Samir, M., Geioushy, R.A., El, S., Osama, S., 2022. Enhancing the anti - ageing , antimicrobial activity and mechanical properties of surface - coated paper by Ag @ TiO 2 - modified nanopigments. Environ. Sci. Pollut. Res. 72515–72527. https://doi.org/10.1007/s11356-022-20935-2.

[15] Costa, J.R.C., Correia, C., Góis, J.R., Silva, S.M.C., Antunes, F.E., Moniz, J., Serra, A.C., Coelho, J.F.J., 2017. Efficient dispersion of TiO2 using tailor made poly (acrylic acid) − based block copolymers, and its incorporation in water based paint formulation. Prog. Org. Coating. 104, 34–42. https://doi.org/10.1016/j.porgcoat.2016.12.006.

[16] Hanaor, D.A.H., Sorrell, C.C., 2011. Review of the anatase to rutile phase transformation. J. Mater. Sci. 46, 855–874. https://doi.org/10.1007/s10853-010-5113-0.

[17] Haider, A.J., Al-Anbari, R.H., Kadhim, G.R., Salame, C.T., 2017. Exploring potential environmental applications of TiO2 nanoparticles. Energy Proc. 119, 332–345. https://doi.org/10.1016/j.egypro.2017.07.117.

[18] Haghighatmamaghani, A., Haghighat, F., Lee, C.-S., 2019. Performance of various commercial TiO2 in photocatalytic degradation of a mixture of indoor air pollutants: effect of photocatalyst and operating parameters. Sci. Technol. Built Environ. 25, 600–614. https://doi.org/10.1080/23744731.2018.1556051.

[19] Gaya, U.I., Abdullah, A.H., 2008. Heterogeneous photocatalytic degradation of organic contaminants over titanium dioxide: a review of fundamentals, progress and problems. J. Photochem. Photobiol. C Photochem. Rev. 9, 1–12. https://doi.org/10.1016/j.jphotochemrev.2007.12.003.

[20] Gonçalves, M.C., Pereira, J.C., Matos, J.C., Vasconcelos, H.C., 2018. Photonic band gap and bactericide performance of amorphous sol-gel titania: an alternative to crystalline TiO 2. Molecules 23. https://doi.org/10.3390/molecules23071677.

[21] Thuc, D.Q., Mai, Q.D., Son, N.A., Nguyen, H.A., Pham, A.T., Le, A.T., 2024. Superior UV resistance of unsaturated polyester resin by employing amorphous e-TiO2 nanoparticles for outdoor applications. ACS Appl. Polym. Mater. 6, 3179–3191. https://doi.org/10.1021/acsapm.3c02958.

[22] Yinghong, X., Xin, W., Xujie, Y., Lude, L., 2003. Nanometre-sized TiO2 as applied to the modification of unsaturated polyester resin. Mater. Chem. Phys. 77, 609–611. https://doi.org/10.1016/S0254-0584(02)00114-1.

[23] Evora, V.M.F., Shukla, A., 2003. Fabrication, characterization, and dynamic behavior of polyester/TiO2 nanocomposites. Mater. Sci. Eng. A. 361, 358–366. https://doi.org/10.1016/S0921-5093(03)00536-7.

[24] Goodarzi, V., Monemian, S.A., Maleki, F., Angaji, M.T., 2008. In situ radical copolymerization in presence of surface-modified TiO 2 nanoparticles: influence of a double modification on properties of unsaturated polyester (UP) nanocomposites. J. Macromol. Sci., Part B: Phys. 47, 472–484. https://doi.org/10.1080/00222340801955065.

[25] Kosmidis-Papadimitriou, A., Qi, S., Squillace, O., Rosik, N., Bale, M., Fryer, P.J., Zhang, Z.J., 2021. Characteristics of respiratory microdroplet nuclei on common substrates. Interface Focus 12. https://doi.org/10.1098/rsfs.2021.0044.

[26] Wang, L., Yang, J., Zhu, Y., Li, Z., Sheng, T., Hu, Y.M., Yang, D.Q., 2016. A study of the mechanical and chemical durability of ultra-ever dry superhydrophobic coating on low carbon steel surface. Colloids Surfaces A Physicochem. Eng. Asp. 497, 16–27. https://doi.org/10.1016/j.colsurfa.2016.02.022.

[27] Choi, H.C., Jung, Y.M., Bin Kim, S., 2005. Size Effects in the Raman Spectra of TiO 2 Nanoparticles, vol. 37, pp. 33–38. https://doi.org/10.1016/j.vibspec.2004.05.006.

[28] Ekoi, E.J., Gowen, A., Dorrepaal, R., Dowling, D.P., 2019. Characterisation of titanium oxide layers using Raman spectroscopy and optical profilometry: influence of oxide properties. Results Phys. 12, 1574–1585. https://doi.org/10.1016/j.rinp.2019.01.054.

[29] Alhomoudi, I.A., Newaz, G., 2009. Residual stresses and Raman shift relation in anatase TiO2 thin film. Thin Solid Films 517, 4372–4378. https://doi.org/10.1016/j.tsf.2009.02.141.

[30] Bonne, M., Pronier, S., Batonneau, Y., Can, F., Courtois, X., Royer, S., Marécot, P., Duprez, D., 2010. Surface properties and thermal stability of SiO2-crystalline TiO2 nano-composites. J. Mater. Chem. 20, 9205–9214. https://doi.org/10.1039/c0jm01184c.

[31] Glaspell, G.P., Zuo, C., Jagodzinski, P.W., 2005. Surface enhanced raman spectroscopy using silver nanoparticles: the effects of particle size and halide ions on aggregation. J. Clust. Sci. 16, 39–51. https://doi.org/10.1007/s10876-005-2714-x.

[32] Gómez, D.A., Coello, J., Maspoch, S., 2019. The influence of particle size on the intensity and reproducibility of Raman spectra of compacted samples. Vib. Spectrosc. 100, 48–56. https://doi.org/10.1016/j.vibspec.2018.10.011.

[33] Durante, O., Di Giorgio, C., Granata, V., Neilson, J., Fittipaldi, R., Vecchione, A., Carapella, G., Chiadini, F., De Salvo, R., Dinelli, F., Fiumara, V., Pierro, V., Pinto, I. M., Principe, M., Bobba, F., 2021. Emergence and evolution of crystallization in tio2 thin films: a structural and morphological study. Nanomaterials 11, 1–18. https://doi.org/10.3390/nano11061409.

[34] Brandt, I.S., Plá Cid, C.C., Azevedo, C.G.G., Pereira, A.L.J., Benetti, L.C., Ferlauto, A.S., Dias Da Silva, J.H., Pasa, A.A., 2018. Influence of substrate on the structure of predominantly anatase TiO2 films grown by reactive sputtering. RSC Adv. 8, 7062–7071. https://doi.org/10.1039/c7ra10974a.

[35] Ben, M., Weththimuni, M.L., Messaoud, M., Urzi, C., Bouaziz, J., De Leo, F., Licchelli, M., 2021. Progress in organic coatings Ag-TiO 2/PDMS nanocomposite protective coatings : synthesis , characterization , and use as a self-cleaning and antimicrobial agent. Prog. Org. Coating. 158, 106342. https://doi.org/10.1016/j.porgcoat.2021.106342.

[36] El-Desoky, M.M., Morad, I., Wasfy, M.H., Mansour, A.F., 2020. Synthesis, structural and electrical properties of PVA/TiO2 nanocomposite films with different TiO2 phases prepared by sol–gel technique. J. Mater. Sci. Mater. Electron. 31, 17574–17584. https://doi.org/10.1007/s10854-020-04313-7.

[37] Gittings, S., Turnbull, N., Henry, B., Roberts, C.J., Gershkovich, P., 2015. Characterisation of human saliva as a platform for oral dissolution medium development. Eur. J. Pharm. Biopharm. 91, 16–24. https://doi.org/10.1016/j.ejpb.2015.01.007.

[38] Labat, F., Baranek, P., Adamo, C., 2008. Structural and electronic properties of selected rutile and anatase TiO2 surfaces: an ab initio investigation. J. Chem. Theory Comput. 4, 341–352. https://doi.org/10.1021/ct700221w.

[39] Daniels, G.C., Iezzi, E.B., Fulmer, P.A., Wynne, J.H., 2016. Progress in organic coatings synergistic antimicrobial and surface free energy of sol – gel coatings containing fluorosilanes and quaternary ammonium salts. Prog. Org. Coatings. 95, 91–99. https://doi.org/10.1016/j.porgcoat.2016.02.021.

[40] Shoaib, M., Latif, Z., Ali, M., Al-Ghamdi, A., Arshad, Z., Wageh, S., 2023. Room temperature synthesized TiO2 nanoparticles for two-folds enhanced mechanical properties of unsaturated polyester. Polymers 15. https://doi.org/10.3390/polym15040934.

[41] Li, J., Sun, Y., Sun, X., Qiao, J., 2005. Mechanical and corrosion-resistance performance of electrodeposited titania - Nickel nanocomposite coatings. Surf. Coating. Technol. 192, 331–335. https://doi.org/10.1016/j.surfcoat.2004.04.082.

[42] Grząbka-Zasadzińska, A., Piątek, A., Klapiszewski, Ł., Borysiak, S., 2024. Structure and properties of polylactide composites with TiO2–Lignin hybrid fillers. Int. J. Mol. Sci. 25. https://doi.org/10.3390/ijms25084398.

[43] Kumar, A., Duhan, S., 2023. In: Antibacterial and Anti-fungal Coating, first ed. Elsevier Ltd. https://doi.org/10.1016/B978-0-323-95169-2.00003-1

[44] Arrieta, M.P., Peltzer, M.A., López, J., Garrigós, M.D.C., Valente, A.J.M., Jiménez, A., 2014. Functional properties of sodium and calcium caseinate antimicrobial active films containing carvacrol. J. Food Eng. 121, 94–101. https://doi.org/10.1016/j.jfoodeng.2013.08.015.

[45] Tran, H.V., Tran, L.D., Ba, C.T., Vu, H.D., Nguyen, T.N., Pham, D.G., Nguyen, P.X., 2010. Synthesis, characterization, antibacterial and antiproliferative activities of monodisperse chitosan- based silver nanoparticles. Colloids Surfaces A Physicochem. Eng. Asp. 360, 32–40. https://doi.org/10.1016/j.colsurfa.2010.02.007.

[46] Babaladimath, G., Badalamoole, V., 2019. Silver nanocomposite hydrogel of Gum Ghatti with potential antibacterial property. J. Macromol. Sci. Part A Pure Appl. Chem. 56, 952–959. https://doi.org/10.1080/10601325.2019.1619462.

[47] Akhter, R., Masoodi, F.A., Wani, T.A., Rather, S.A., 2019. Functional characterization of biopolymer based composite film: incorporation of natural essential oils and antimicrobial agents. Int. J. Biol. Macromol. 137, 1245–1255. https://doi.org/10.1016/j.ijbiomac.2019.06.214.

[48] Pourhashem, S., Saba, F., Duan, J., Rashidi, A., Guan, F., Nezhad, E.G., Hou, B., 2020. Polymer/inorganic nanocomposite coatings with superior corrosion protection performance: a review. J. Ind. Eng. Chem. 88, 29–57. https://doi.org/10.1016/j.jiec.2020.04.029.

[49] Molaei, M., Fattah-Alhosseini, A., Nouri, M., Kaseem, M., 2023. Role of TiO2 nanoparticles in wet friction and wear properties of PEO coatings developed on pure titanium. Metals 13. https://doi.org/10.3390/met13040821.